JOURNAL OF AIRCRAFT
Vol. 50, No. 5, September–October 2013

Determining Aerodynamic Characteristics of a Micro Air Vehicle Using Motion Tracking

Daniel V. Uhlig* and Michael S. Selig†
University of Illinois at Urbana–Champaign, Urbana, Illinois 61801

DOI: 10.2514/1.C031996

The aerodynamic performance of small-scale fixed-wing flight is not well understood, and flight data is needed to gain a better understanding of the aerodynamics of micro air vehicles. The flight characteristics of micro air vehicles are difficult to measure because the small size and low weight prevent the use of conventional onboard instrumentation systems. In this research, an offboard motion tracking system captured the motion trajectory during the flights of a small off-the-shelf radio-controlled airplane that weighed 14.44 g (0.5094 oz) and had a span of 37.47 cm (14.75 in.). The recorded motion-path time histories were analyzed to determine the aerodynamic characteristics of the airplane during unpowered flight. The results presented show the longitudinal aerodynamic characteristics of the micro air vehicle over a wide range of angles of attack at a nominal Reynolds number of 25,000. Specifically, lift and drag characteristics of the airplane were obtained from the analysis of the flight trajectories during quasi-steady nominal gliding flight, as well as unsteady high angle-of-attack flight. The nominal-gliding flights showed an almost linear lift curve and small unsteady effects that were in part due to the angle-of-attack rate. During the unsteady high angle-of-attack flight, as would be seen during perching maneuvers, deep stall maneuvers, and highly dynamic flight in confined spaces, the unsteady effects of rapid changes in the angle of attack significantly increased the lift coefficient during pitch-up maneuvers and then decreased the lift coefficient during pitch-down maneuvers. By using numerous flight tests in both regimes (nominal-gliding and unsteady high angle-of-attack flight), the results show the effect of the angular rate and expand on the limited existing work. The flight-test results presented show the influence of unsteady aerodynamic effects on the longitudinal aerodynamic characteristics of a micro air vehicle in both quasi-steady nominal gliding flight and unsteady high angle-of-attack flight.

Nomenclature

AR	=	aspect ratio
a	=	semichord
b	=	wingspan
C_D	=	drag coefficient ($D/\frac{1}{2}\rho V^2 S_{\text{ref}}$)
C_{D_o}	=	parasite drag coefficient
C_L	=	lift coefficient ($L/\frac{1}{2}\rho V^2 S_{\text{ref}}$)
C_{L_α}	=	airplane lift curve slope
C_{l_α}	=	airfoil lift curve slope
C_M	=	pitching moment coefficient ($M/\frac{1}{2}\rho V^2 S_{\text{ref}} c$)
c	=	wing mean aerodynamic chord
D	=	drag force
e_o	=	Oswald efficiency factor
$\mathbf{F}$	=	force vector
K	=	constant for induced drag coefficient
k	=	reduced frequency ($\dot{\alpha}c/2V$)
L	=	lift force
m	=	airplane mass
p, q, r	=	roll, pitch, and yaw rates
Re	=	Reynolds number based on mean aerodynamic chord (Vc/ν)
S_{ref}	=	wing reference area
u, v, w	=	body-fixed translational velocity
V	=	inertial speed
$\bar{x}$	=	distance normalized by the wing root chord
α	=	angle of attack (referenced to fuselage)
$\dot{\alpha}$	=	angle-of-attack rate
β	=	sideslip angle
$\dot{\beta}$	=	rate of change of sideslip angle
ν	=	kinematic viscosity
ρ	=	density of air
ϕ, θ, ψ	=	roll, pitch, and heading angles
ω	=	angular rates

Subscripts

ac	=	aerodynamic center
cg	=	center of gravity
h	=	property of the stabilator
trim	=	property at trim flight conditions
w	=	property of the wing

Presented as Paper 2010-8416 at the AIAA Guidance, Navigation, and Control Conference, Toronto, Ontario, 2–5 August 2010; received 11 June 2012; revision received 19 February 2013; accepted for publication 22 February 2013; published online 8 July 2013.

*Graduate Student, Department of Aerospace Engineering, 104 S. Wright St. Student Member AIAA.

†Associate Professor, Department of Aerospace Engineering, 104 S. Wright St. Senior Member AIAA.

I. Introduction

ALTHOUGH there is a growing use of micro air vehicles (MAVs), accurate and detailed aerodynamic data in the Reynolds numbers range from 5,000 to 40,000 is limited. To better model MAV aerodynamic performance, further testing is needed to refine the models and predictions of airplane performance. The complexity of low Reynolds number flow can be observed from the test results of airfoils and wings at Reynolds number below 500,000 [1–8]. At lower Reynolds numbers (less than 100,000), limited results are available, and low Reynolds number effects, such as decreased lift slope, increased profile drag, and the presence of laminar separation bubbles become more pronounced [9–11].

Free-flight testing can aid in measuring the aerodynamic characteristics of MAVs [12]. Using modern motion tracking techniques, the forces acting on MAVs can be determined from flight data [13,14]. In addition, motion tracking can be used to measure unsteady effects without the complex apparatus that is normally required in wind-tunnel tests [15,16]. To understand the effect of large angular rates on aerodynamic characteristics, more extensive studies are needed to build on the limited existing work [15,16]. Understanding the effect of angular rates is particularly important at this scale

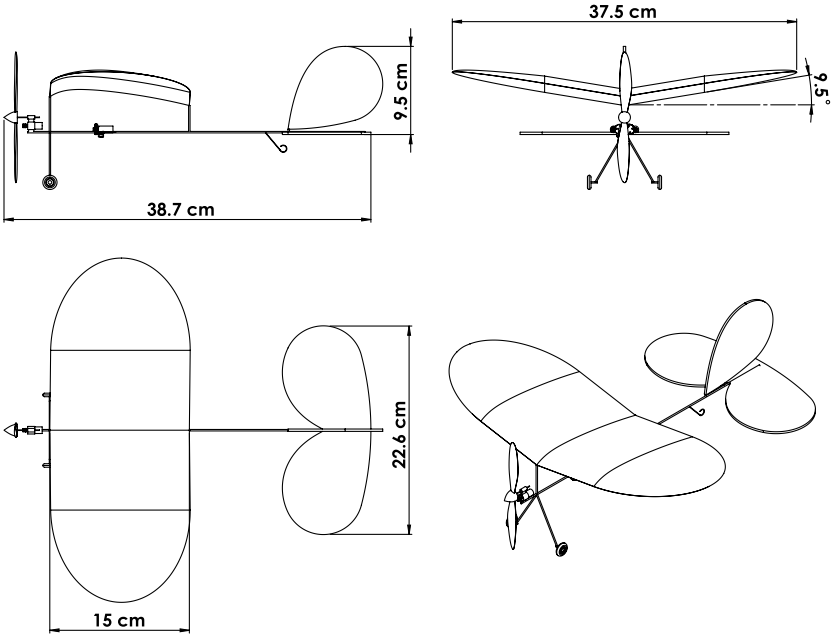

Fig. 1 A three-view drawing showing the geometry of the test aircraft.

because MAVs operate over a large flight envelope owing to their high maneuverability and their exposure to large sideslip and angle-of-attack excursions in windy conditions.

This paper presents the experimentally measured lift and drag characteristics for a MAV in free flight. The test airplane weighed 14.44 g (0.5094 oz) and flew at a nominal Reynolds number of approximately 25,000. The results for the complete airframe show the aerodynamic characteristics of the MAV over a large range of angles of attack and are more extensive than previously reported results. The results in the nominal-gliding regime are compared with theory, and the results from the unsteady flights are used to highlight the effects of longitudinal motion on the aerodynamic forces.

II. Experimental Apparatus

Figure 1 shows a three-view drawing of the commercially available Vapor airplane [17] that was tested. The MAV had a 37.47 cm (14.75 in.) wingspan and weighed 14.44 g (0.5094 oz). The airframe was constructed with carbon fiber supports and cambered ribs for the main wing. A thin plastic film was stretched over the wing and tail structures to form membrane aerodynamic surfaces. The physical properties of the MAV were measured and are tabulated in Table 1. A small battery-powered radio-controlled receiver controlled the electric motor and two servos that actuated the all-moving tail surfaces: a flat-plate stabilator and vertical fin. In these tests, the receiver was not used to actuate the control surfaces in flight, but it was used before a flight to set the incidence of the stabilator in order to control the trim speed.

Vicon camera systems [18] have been used by robotics researchers to triangulate and track small aircraft. In this research, eight infrared Vicon T20 cameras tracked the reflections from circular markers, and the software provided by Vicon triangulated the location of the reflections in the capture volume. The capture volume had a rectangular base of $\approx 3.6 \times 6.1$ m (12×20 ft) and extended to a height of ≈ 3 m (10 ft). The cameras were distributed around the upper perimeter of the capture volume and tracked five reflective markers on the airplane. The reflective markers included spheres [approximately 5 mm (0.2 in.) in diameter] and flat circular stickers [approximately 13 mm (0.5 in.) in diameter]. The reflective markers were spread to the extremities to ensure maximum marker separation, and they were placed asymmetrically to ensure the proper triangulation of the position and attitude of the aircraft. Two spherical markers were placed along the centerline of the fuselage with one just forward of the horizontal tail. The other spherical marker was placed on the trailing edge of the wing centerline. Three additional circular sticker-type markers were spread over the wing with one at the left wing tip, one on the trailing edge of the right wing at 95% of the semispan, and one on the leading edge of the right wing at 50% of the semispan. A recording rate of 200 Hz was used to capture the tracking data.

To track the flight trajectory of the MAV with software, a skeletal graphical model was constructed. The model used multiple markers to define the objects that represented each component of the MAV to be tracked, specifically the wing, fuselage, stabilator, and vertical fin. For each object, the Earth-referenced position and the Euler angles were recorded by the system. Whenever the system could not triangulate the object (less than 0.7% of the time), there was a measurement void in the trajectory time history.

Trajectory data were taken from free-flight glides (no thrust and uncommanded) that started from a hand launch. Gliding flights were used to eliminate the additional complexity of propeller effects. These numerous flight tests collectively covered a range of flight conditions including quasi-steady glides, stalls (covering the range from mild to aggressive), and stall recoveries. The airplane flight trajectory was controlled by adjusting the launch speed, launch angle, and the incidence of the horizontal stabilator. Trajectory time histories were limited by the size of the capture volume, yielding 2–3 s of useful data for a given flight. By combining multiple tests, a detailed model of the airplane aerodynamic characteristics was developed.

Table 1 Physical properties of the MAV

Parameter	Value	
Mass	14.44 g	(0.5094 oz)
Wing		
Span	37.47 cm	(14.75 in.)
Area, S_{ref}	546.3 cm^2	(84.67 in^2)
Chord (at root)	15.0 cm	(5.90 in.)
Aspect ratio, AR	2.56	
Incidence angle	3.0 deg	
Dihedral	9.5 deg	
Airfoil camber	6.7%	
Length	38.74 cm	(15.25 in.)
Stabilator area, S_h	175.9 cm^2	(27.27 in^2)
Vertical fin area	99.87 cm^2	(15.48 in^2)

III. Data Acquisition and Postpocessing

A. Calculating Aerodynamic Properties from the Motion Track

The aerodynamic forces acting on the airplane were determined by postprocessing the trajectory time history data for each flight to determine the aerodynamic characteristics throughout flight. Raw measurements in the Earth-referenced coordinate system were transformed into attitude, angular rates, velocities, and accelerations in the body-fixed axes system to determine the aerodynamic characteristics.

In postprocessing, the first step was to fill the voids (the periods during which the system was unable to triangulate the MAV) by estimating the attitude and position using linear interpolation based on the neighboring points in the trajectory time history. After filling in these points, the raw measurements were smoothed using a third-order polynomial regression (Savitzky–Golay) method [19,20]. During the smoothing process, the third-order polynomial fit that was used for smoothing was differentiated twice to calculate the first and second derivative of the Earth-referenced position and attitude time histories. The derivatives from the polynomial regression results were then used to determine the forces and moments acting on the airplane in the body-fixed frame.

From the smoothed and differentiated data, the flow angles of the airplane were found from

$$\alpha = \tan^{-1}(w/u) \tag{1a}$$

$$\beta = \sin^{-1}(v/V) \tag{1b}$$

The inertial speeds were used in Eqs. (1a) and (1b) to estimate the freestream flow angles under the assumptions that the air in the test volume was quiescent and that induced flow effects were negligible. Time derivatives of the angles were taken to yield $\dot{\alpha}$ and $\dot{\beta}$. The angle-of-attack rate $\dot{\alpha}$ was nondimensionalized using the mean aerodynamic chord c and the total velocity V, that is

$$k = \frac{\dot{\alpha}c}{2V} \tag{2}$$

which can be referred to as the reduced frequency and is a measure of the degree of unsteadiness in the flow. A magnitude of the reduced frequency of less than 0.05 is referred to as quasi-steady because the unsteady effects are generally small [21]. At larger values of reduced frequency, the unsteady effects can have a significant influence on the aerodynamics.

Accelerations obtained from the motion track were then used to find the total external force $\mathbf{F}_{\text{ext}}$ acting on the aircraft in the body-fixed frame with x out the nose and y out the right wing. By subtracting the force of gravity $\mathbf{F}_G$ from the total external force, the total aerodynamic force $\mathbf{F}_{\text{aero}}$ acting on the aircraft becomes

$$\mathbf{F}_{\text{aero}} = \mathbf{F}_{\text{ext}} - \mathbf{F}_G \tag{3}$$

The components ($F_{\text{aero},x}$, $F_{\text{aero},y}$, and $F_{\text{aero},z}$) of the total aerodynamic force $\mathbf{F}_{\text{aero}}$ in the body-fixed frame were transformed into the wind axes to obtain lift and drag, that is [22]

$$L = -F_{\text{aero},z}\cos\alpha + F_{\text{aero},x}\sin\alpha \tag{4a}$$

$$D = -F_{\text{aero},z}\sin\alpha\cos\beta - F_{\text{aero},x}\cos\beta\cos\alpha - F_{\text{aero},y}\sin\beta \tag{4b}$$

The resulting time histories of lift and drag in the wind axes were used to determine the aerodynamic characteristics of the aircraft throughout flight.

The moments on the airplane were calculated from the changing attitude of the airplane using

$$\frac{\mathrm{d}(\mathbf{I}\omega)}{\mathrm{d}t} = \mathbf{M}_{\text{ext}} \tag{5}$$

where ω is the body-fixed angular rates (p, q, and r), and $\mathbf{I}$ is the inertia matrix that was determined by measuring the mass distribution. The roll, pitch, and yaw moment components (L, M, and N, respectively) can be determined through the flight trajectory. Only the pitching coefficient about the center of gravity

$$C_{M_{\text{cg}}} = \frac{M}{qS_{\text{ref}}c} \tag{6}$$

is used in this paper.

As one would expect from free-flight testing, minute variations in the launch conditions produced consequent variations in the flight path trajectory. Hence, multiple flight tests were performed in order to quantify and illustrate general trends in the instantaneous measured aerodynamic characteristics, namely lift and drag. Moreover, the flights were mainly straight because the aircraft was trimmed for straight flight and also because the configuration had significant roll and yaw stability by way of the wing dihedral and a vertical fin. Consequently, any sideslip that might have been introduced at launch was quickly nulled. Thus, in the reduced data presented here, the side force and turning flight dynamics were negligible.

B. Measurement Uncertainty

To understand the uncertainty in the aerodynamic characteristics determined from the captured motion trajectory, the accuracy of the tracking system measurements was quantified through a variety of tests. First, stationary tests were used to analyze the noise within the measurements. Second, a rotating rod attached to an optical encoder was used to verify angular measurements during motion. Third, repeatability tests showed that the aerodynamic characteristics of a glider were consistent across repeated launches. Although uncertainty exists within the final results, the tests show how the system can be used to measure the aerodynamic forces.

For the stationary tests, the airplane with markers attached was positioned at rest in the motion capture volume. The time histories of the position and attitude were recorded, and the standard deviation in each axis was calculated. Figure 2 shows the time history of the position and attitude from a 2.5 s stationary test recorded at 200 Hz. From the results, the standard deviation for the distance measurement was 0.079 mm (0.0031 in.), and the standard deviation for the norm of the Euler angle vector was 0.034 deg. The standard deviation for all of the components of the position and attitude are listed in Table 2. A similar noise analysis found in the literature [16] showed similar uncertainties when measuring at 100 Hz. The uncertainties from Mettler's analysis [16] were of the same order of magnitude as the current research, with the current research having a smaller standard deviation in the measurements. The difference in the uncertainties could be due to the differences in the recording frequency and the differences in marker separation because the airplane in [16] was half the size of the MAV in this research.

In addition to the stationary test, a rotating rod was tracked to quantify the uncertainty of the motion tracking system during simple motion. The rod rotated about one end that was attached to an optical rotary encoder that provided data for comparison with the captured motion trajectory. The data from the optical encoder were recorded at 512 Hz using an US Digital H6-1800-I-S optical encoder having an accuracy of 0.05 deg [23]. Reflective markers were attached to the center of rotation and the tip of the rod. The two markers were 25.78 cm (10.15 in.) apart. The motion track of the tip of the rod formed an arc, and the angle of the rod was recorded with the motion tracking system.

Figure 3 shows a comparison of the optical encoder data with the results from the recorded motion trajectory. During the stationary portion (the first $\approx$0.5 s), the residual is within $\pm$0.04 deg. The uncertainty range is similar to that shown in Fig. 2b for the attitude of the stationary aircraft. When the rod started to rotate, the residual peaked and was almost an order of magnitude larger than the

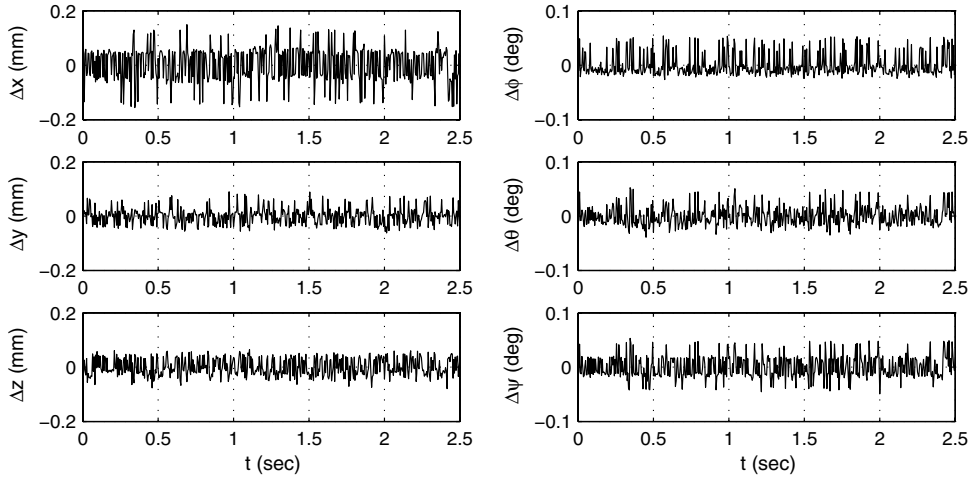

a) b)

Fig. 2 The 2.5 s time history of the a) position and b) attitude of the stationary airplane showing minute measurement noise.

stationary tests. Once steady motion was established (after $t \approx 1$ s), the residual decreased to ± 0.06 deg, which is slightly larger than during the stationary portion of the test.

The final system verification method involved repeatability tests with a small glider. The tests were conducted using a rail launching system to achieve consistent initial flight conditions for a glider. The glider weighed approximately 8.738 g (0.3082 oz) and operated at a Reynolds number of approximately 16,000 [24]. The launch rail was placed at an inclined angle, and a cart carrying the airplane was accelerated down the track by a falling weight. At the end of the track, the cart fell down and separated from the airplane as the airplane started to glide. The launch conditions could be adjusted by changing the acceleration of the cart and the angle of the track incline. By repeating launches with the same conditions, a set of initial conditions could be repeated across multiple flights, and the repeatability of the measurements from the system could be gauged by examining the flight conditions and the determined aerodynamic characteristics of the airplane.

Figure 4 shows the height of the airplane as a function of the distance traveled during six rail-launched flights. The small triangle approximates the beginning of the rail, and the small square approximates where the airplane separated from the cart and started to glide. The six flights had the same launch conditions starting at a height of approximately 1.8 m (6 ft) and ending on or close to the floor. Each of the trajectories follows a similar path with some variation caused by small variations in the initial conditions.

By processing multiple flight trajectories with repeated launch conditions, the lift and drag coefficient data were calculated. Figure 5 shows the result for five flights with each flight indicated by a different marker shape. The lift curve and drag polar follow similar trends for all five of the flights. All of the flights started at higher angles of attack before settling at a trim angle of attack of approximately 4 deg, and all of the flights had similar lift and characteristics. The flight tests showed the repeatability of the aerodynamic characteristics determined from the captured flight trajectories.

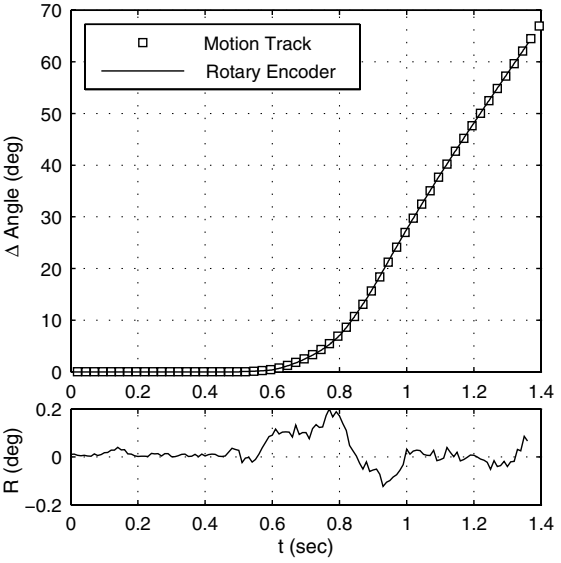

Fig. 3 Angular measurements from the motion tracking system compare with measurements from an optical rotary encoder.

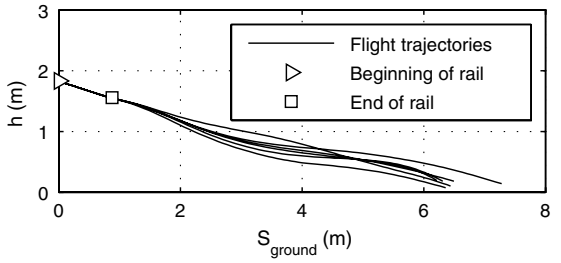

Fig. 4 A plot showing the distance traveled of six different repeatability tests. The triangle and square markers show the location of the start and end of the launching rail, respectively.

Table 2 Standard deviation of the position and attitude components for a stationary 2.5 s motion track recorded at 200 Hz

Trajectory component	Standard deviation		
Position, mm	x	y	z
	0.0650	0.0303	0.0329
Attitude, deg	ϕ	θ	ψ
	0.0207	0.0175	0.0208

IV. Results and Discussion

The numerous MAV glide flight tests of the Vapor were divided into two sets. The first set can be characterized as quasi-steady nominal gliding flight, in which the angle of attack varied from −5 to 20 deg, which was below stall for the airplane. The flight conditions were close to steady state but included small angular rates with the reduced frequency staying below 0.05. The second set of flights were characterized as being substantially unsteady over a much larger angle-of-attack range (−10 to 90 deg) thereby including stalls that

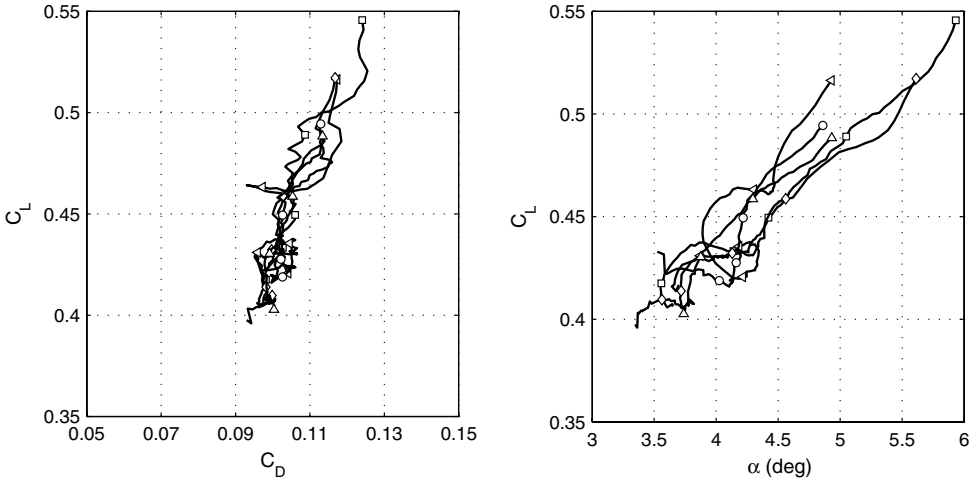

Fig. 5 The a) drag polar and b) the lift curve during five repeatability flights.

varied from mild to aggressive (maximum k above 0.4). The time histories of various flight parameters, such as C_L, C_D, α, and $\dot{\alpha}$ were determined for each flight trajectory. The lift and drag forces [Eqs. (4a) and (4b)] at each instant in time were nondimensionalized by S_{ref} and the instantaneous dynamic pressure determined from the motion tracking flight speed.

A. Quasi-Steady Nominal Gliding Flights

Figure 6 shows all 14 trajectories of the quasi-steady flights (the trajectories labeled A and B are addressed later with Figs. 7 and 8). No changes were made to the control surfaces during flight, but between some of the flights, the elevator deflection was varied to change the trim speed. The time histories were truncated when the airplane either approached landing or flew out of the capture volume. Figure 7 shows the lift curve during two of the quasi-steady flights taken at the recording rate of 200 Hz (with markers being plotted every eighth point). These two flights are also labeled in Fig. 6. Figure 8 shows the reduced frequency as a function of the angle of attack during both flights. The starting points for the flights A and B are shown in Fig. 7. For flight A, the angle of attack decreases gradually with a peak k value of ≈ -0.09. Flight B initially has a positive k value and after the angle of attack peaks, the angle of attack decreases with a peak k value of ≈ -0.015. The lift curve for flight B (Fig. 7) shows a greater value of C_L during the pitch-up portion of flight and a decrease in C_L during the pitch-down portion. Although both flights are well within the reduced frequency bounds (± 0.05) for quasi-steady [21] angular rates, the difference in the lift curve exhibited during the two flights shows the effect of relatively low angular rates on MAV aerodynamic characteristics. The effect of the reduced frequency during all of the quasi-steady flights is further explained later in the paper.

Expanding on the results for the two flight tests just discussed, Fig. 9 shows the drag polar and lift curve for 14 of the quasi-steady flights. As previously discussed, unsteady aerodynamic effects are present in the data because of the variation in $\dot{\alpha}$ during the different flights. The 14 nominal quasi-steady trajectories were conditionally-sampled so that only time history segments with the lowest angular rates (<30 deg/s or a nominal k value of ≈0.012) were used to fit the lift curve and drag polar. By removing the data points from the quasi-steady flights with larger angular rates, the effect of $\dot{\alpha}$ could be

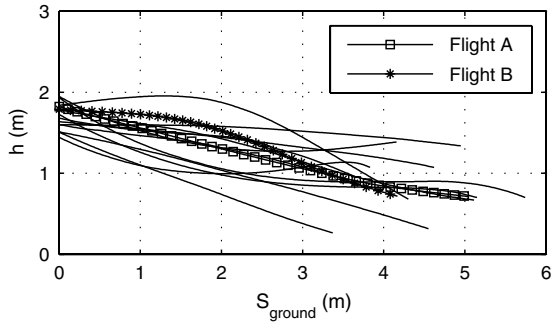

Fig. 6 The quasi-steady flight trajectories of the MAV (flights A and B are referenced in Figs. 7 and 8).

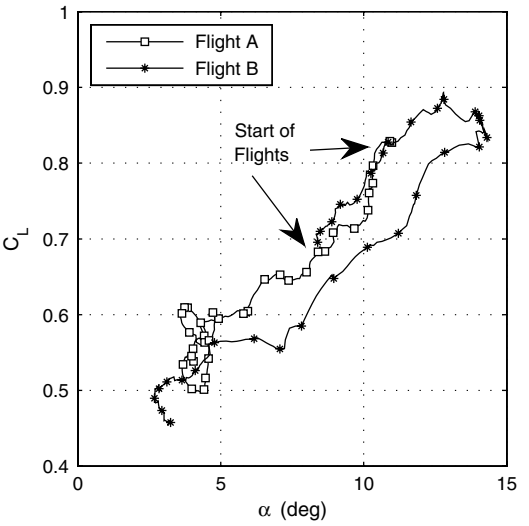

Fig. 7 Experimentally determined lift curve for two of the quasi-steady flights (see Fig. 6).

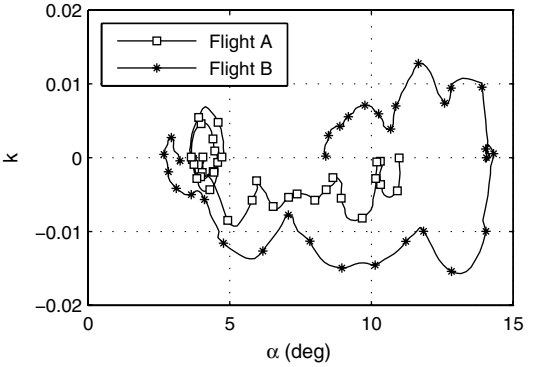

Fig. 8 The reduced frequency as a function of the angle of attack for two of the quasi-steady flights (see Fig. 6).

decreased, and the results would be closer to steady-state conditions. Figure 10 shows the conditionally-sampled low-angular rate data with a least-squares parabolic fit to the drag polar and a linear fit to the lift curve.

Figure 10a shows the drag polar for the conditionally-sampled experimental data, along with a parabolic drag polar fit of the form

$$C_D = C_{D_o} + KC_L^2 \tag{7}$$

where KC_L^2 is the induced drag of the airplane, that is

$$C_{D_i} = \frac{C_L^2}{\pi e_o \mathrm{AR}} \tag{8}$$

which depends on the aspect ratio AR and the Oswald efficiency factor e_o. The parabolic fit over the C_L range of 0–1.1 is $C_D = 0.054 + 0.26C_L^2$. With K from the parabolic fit ($K = 0.26$), Eq. (8) can be used to determine the Oswald efficiency factor from

$$e_o = \frac{1}{\pi K \mathrm{AR}} \tag{9}$$

For the MAV tested, e_o was determined to be 0.48 for the entire aircraft having a wing aspect ratio of 2.56. The value is low and similar to other measurements at low Reynolds numbers. Specifically, Spedding and McArthur [11] determined e_o to be 0.53 from wind-tunnel results for an aspect ratio 6 wing at a Reynolds number of 20,000.

B. Wing Lift Calculations

The lift coefficient data shown previously were for the entire MAV and thereby included the aerodynamic force of the stabilator. The lift coefficient for just the wing is required to compare the results with theoretical calculations. The lift of the entire MAV depends on both the wing and the stabilator [25], viz

$$C_L = C_{L_w} + C_{L_h}\eta_h \frac{S_h}{S_{\mathrm{ref}}} \tag{10}$$

where η_h is the dynamic pressure ratio at the tail and taken to be 0.9 [26]. The reference areas S_{ref} and S_h are given in Table 1. The pitching moment $C_{M_{\mathrm{cg}}}$ is given by

$$C_{M_{\mathrm{cg}}} = C_{M_{\mathrm{ac},w}} + C_{L_w}(\bar{x}_{\mathrm{cg}} - \bar{x}_{\mathrm{ac},w}) - C_{L_h}\eta_h \frac{S_h}{S_{\mathrm{ref}}}(\bar{x}_{\mathrm{ac},h} - \bar{x}_{\mathrm{cg}}) \tag{11}$$

where the center of gravity $\bar{x}_{\mathrm{cg}}$ was measured to be 36% of the wing root chord, and the aerodynamic center of the wing $\bar{x}_{\mathrm{ac},w}$ and the tail $\bar{x}_{\mathrm{ac},h}$ were approximated to be located at 25% of the mean aerodynamic chord for each respective surface. The pitching moment

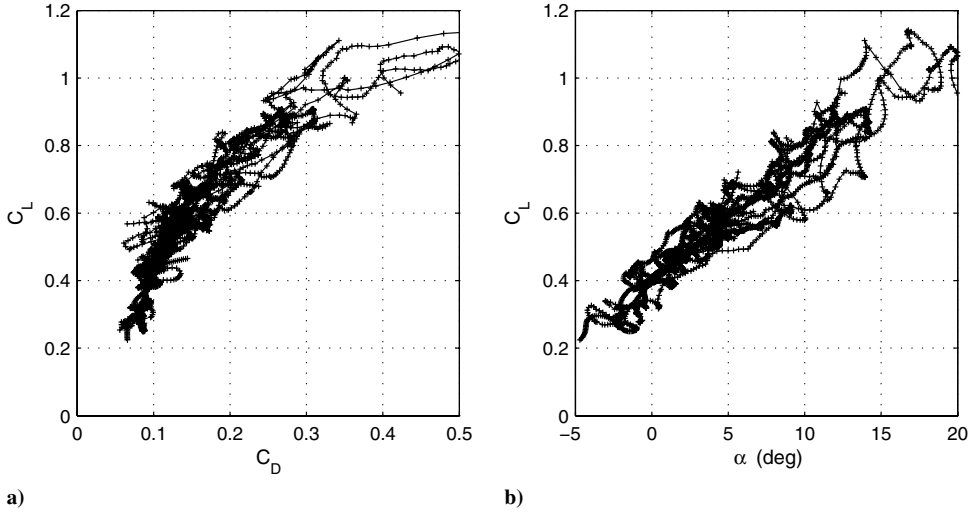

Fig. 9 Experimentally determined a) drag polar and b) lift curve for the quasi-steady flights.

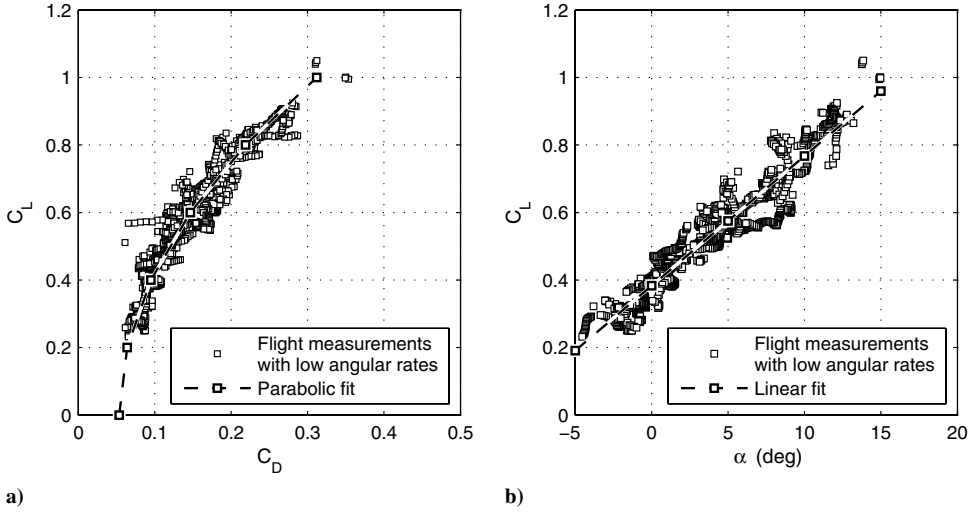

Fig. 10 Experimentally determined a) drag polar and b) lift curve for the conditionally-sampled low-angular rate quasi-steady flight data along with the parabolic drag polar fit and linear lift curve fit.

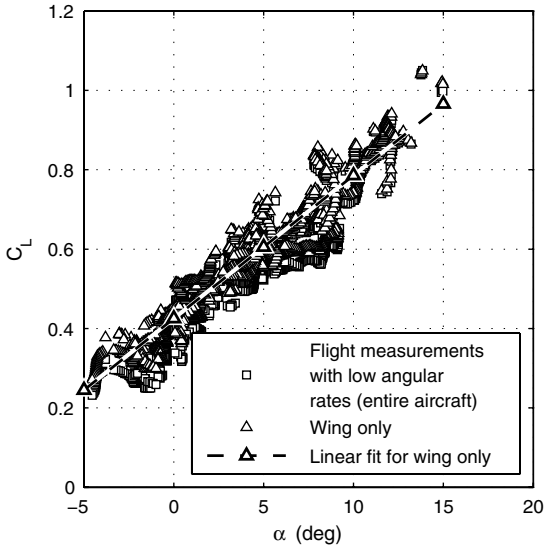

Fig. 11 The lift coefficient of the wing compared the lift coefficient for the entire aircraft during the conditionally-sampled quasi-steady flights.

of the wing $C_{M_{\text{ac},w}}$ was estimated to be −0.12 based on XFOIL[‡] results for a generic thin 6.7% cambered airfoil and experimental results [7] for a thin cambered airfoil (such as the GOE 417A). The values for $C_{M_{\text{ac},w}}$ were found to vary from −0.09 to −0.15, depending on the angle of attack and Reynolds number. The lift curve slope did not vary with different values of the wing pitching moment. However, the wing lift coefficient at zero angle of attack depended on the value of $C_{M_{\text{ac},w}}$

During flight, $C_{M_{\text{cg}}}$ and C_L for the airplane were determined from the flight trajectory [see Eqs. (4a) and (6)]. In Eqs. (10) and (11), the only remaining unknowns are the wing C_{L_w} and the tail C_{L_h}. Solving the two equations simultaneously results in

$$C_{L_h} = \frac{C_{M_{\text{ac},w}} - C_{M_{\text{cg}}} + C_L(\bar{x}_{\text{cg}} - \bar{x}_{\text{ac},w})}{\frac{S_h}{S_{\text{ref}}}\eta_h(\bar{x}_{\text{ac},h} - \bar{x}_{\text{ac},w})} \tag{12a}$$

$$C_{L_w} = \frac{C_{M_{\text{cg}}} - C_{M_{\text{ac},w}} + C_L(\bar{x}_{\text{ac},h} - \bar{x}_{\text{cg}})}{(\bar{x}_{\text{ac},h} - \bar{x}_{\text{ac},w})} \tag{12b}$$

Using $C_{M_{\text{cg}}}$ and C_L from the trajectory time histories, Fig. 11 shows C_L for the entire aircraft and C_{L_w} from Eq. (12b) for the conditionally-sampled quasi-steady flight data (shown in Fig. 10b). A linear fit was used to determine the lift curve slope for both cases. The lift curve slope for the entire aircraft is 2.21/rad (shown in Fig. 10b), and the lift curve slope for the wing alone is 2.06/rad (shown in Fig. 11). The calculated lift of the wing was less than the lift of the entire aircraft, which indicates a lifting stabilator. With the lift slope of the wing known, the results can be compared with the theoretical lifting line results.

The measured wing lift curve slope of 2.06/rad can be compared with predictions using the wing aspect ratio of 2.56. A predicted lift curve slope of 3.52/rad is obtained using a classic lifting line theory, that is

$$C_{L_\alpha} = 2\pi\left(\frac{\text{AR}}{\text{AR} + 2}\right) \tag{13}$$

However, a lower lift curve slope of 3.06/rad is found using the more applicable low aspect ratio Helmbold equation given by

$$C_{L_\alpha} = 2\pi\left(\frac{\text{AR}}{2 + \sqrt{4 + \text{AR}^2}}\right) \tag{14}$$

Both of these results from the theory [with Eq. (14) being more appropriate for the aspect ratio] overpredicted the lift curve slope, and the difference is ascribed primarily to low Reynolds number viscous effects. This decrease is expected and has been shown in various wind-tunnel results. The experimental lift curve slope was 67% of the theoretical value from the Helmbold equation, which is similar to the decrease seen in [11] for the Reynolds numbers of 20,000 and 30,000. These flight test results continue to demonstrate the decrease in the lift curve slope that other researchers have observed in wind-tunnel experiments.

C. Reduced Frequency Effect

As previously mentioned, the angle-of-attack rate influences the lift during the quasi-steady flights. A model for the effect of k on the lift coefficient during quasi-steady motion models the varying angle of attack as a change in the effective camber of the airfoil, which increments the lift coefficient [21]. The increment in the lift coefficient can be described as

$$\Delta C_{l,k} = 2\pi k\left(\frac{1}{2} - a\right) \tag{15}$$

where $a = -1$ is at the leading edge, 1 is at the trailing edge, and, thus, $a = -0.5$ is at the wing quarter chord, the latter of which was used for the following calculations. The change in lift due to the unsteady effects $\Delta C_{l,k}$ is additive to the steady-state lift curve. Once the two-dimensional unsteady lift is known, the three-dimensional unsteady lift is found using

$$\Delta C_{L,k} = \frac{C_{L_\alpha}}{C_{l_\alpha}}\Delta C_{l,k} \tag{16}$$

where C_{l_α} is 2π, and C_{L_α} is the lift curve slope for the entire aircraft. When combined with Eq. (15), Eq. (16) becomes

$$\Delta C_{L,k} = C_{L_\alpha} k\left(\frac{1}{2} - a\right) \tag{17}$$

which uses the experimentally determined lift curve slope for the entire aircraft. Although the result is based on thin airfoil theory, which overpredicts the lift curve slope at low Reynolds number, the method provides an estimate of the incremental lift due to quasi-steady effects. In addition, the final result in Eq. (17) uses the experimentally determined lift curve slope (of the entire aircraft) to avoid problems of overprediction. In the following paragraph, an estimate of the change in lift $\Delta C_{L,k}$ is found using Eq. (17), and the results based on the theory are compared with the experimental results.

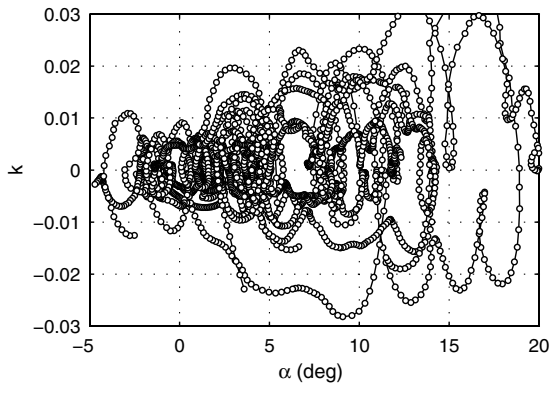

Fig. 12 The reduced frequency during all 14 quasi-steady flights.

[‡]XFOIL airfoil software available online at http://web.mit.edu/drela/Public/web/xfoil/ [retrieved 19 September 2012].

Figure 12 shows the reduced frequency k as a function of the angle of attack during all of the quasi-steady flights. The flights cover a range of angles of attack and have relatively small values of k as was shown earlier in Fig. 8 for the case of just two flights. A general observation is that although the excursions are within the range of $k \approx \pm 0.03$, the range of the reduced frequency increases with the angle of attack, and this increase is primarily due to the flight dynamics: smaller trajectory excursions at higher speeds (low α) and vice versa. The predicted $\Delta C_{L,k}$ was calculated using Eq. (17) along with the time histories of V and $\dot{\alpha}$. Figure 13 shows the linear lift curve for the entire airplane augmented with the unsteady effects (due to k) calculated from the flight conditions for the complete time histories of the 14 quasi-steady flights. The variation in the lift coefficient in Fig. 13 can be compared with the previously shown quasi-steady experimental data (Fig. 9b). Although both results have similar trends in the variation, the variation in the experimental results is larger than in the predicted results. The standard deviation from the linear lift curve slope for the experimental results is 0.057, whereas for the theoretical results it is only 0.018. The results show how the effective camber model can be used to estimate a component of the quasi-steady influence on MAV lift, but the model underpredicts the influence because it does not include all of the effects of quasi-steady flow. Specifically, the effective camber model only included effects due to k and neglected additional unsteady effects, such as apparent mass, quasi-steady lift from the horizontal tail, and additional effects that might be attributed to low Reynolds number separation bubble dynamics. The results show the influence that $\dot{\alpha}$ has on the lift coefficient of MAVs even in the quasi-steady regime, and that the quasi-steady effective camber model does not predict all of the quasi-steady influences on lift for MAVs.

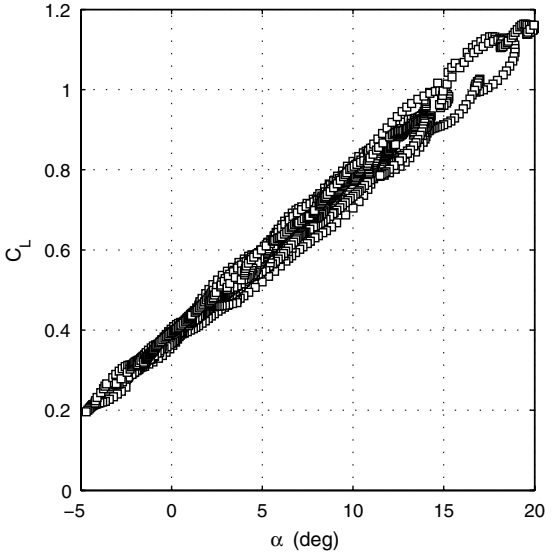

Fig. 13 The linear lift curve model augmented with $\Delta C_{L,k}$ for the quasi-steady flights.

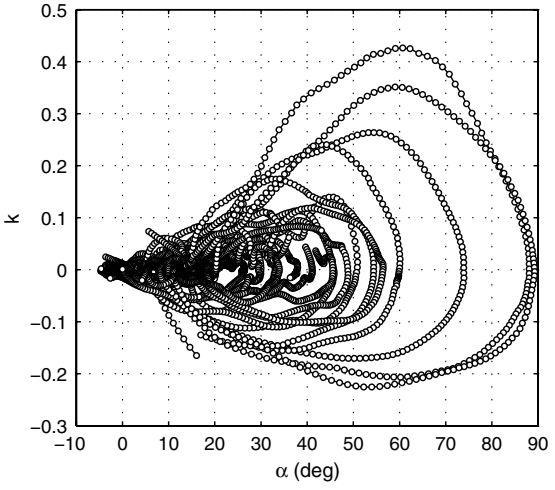

Fig. 14 The reduced frequency for the unsteady flights that include mild to aggressive stalls.

D. Unsteady High Angle-of-Attack Flight

In addition to the quasi-steady flight tests, a second set of data was recorded for flights that covered a wide flight regime to show the lift and drag characteristics at high angles of attack. The flights included brief excursions to high angles of attack and unsteady conditions (due to $\dot{\alpha}$ and translational acceleration). The unsteady flight results depended significantly on $\dot{\alpha}$, and Fig. 14 shows the reduced frequency k as a function of the angle of attack for the unsteady flights. The values of k cover a much larger range (-0.2 to 0.4) than in the previously discussed quasi-steady flight tests.

Figure 15 shows the lift and drag coefficient data for the MAV during the unsteady flight trajectories over an angle-of-attack range from -10 to 90 deg, as well as the previous linear lift curve fit (see Fig. 10b) for comparison. As expected from the unsteady nature of the flights and the large range of k, Fig. 15b shows that C_L varies over a range for each angle of attack. Each flight began with a pitch-up (positive k) that led to stall, and the C_L values were larger than during the subsequent stall recovery (pitch-down maneuver with negative k). The unsteady nature of the flights resulted in a dynamic stall hysteresis loop illustrated by the flights in Fig. 15b, particularly the single selected flight, which will be explained in detail. In Fig. 16, the large positive values of k (pitch-up) increased C_L, whereas the

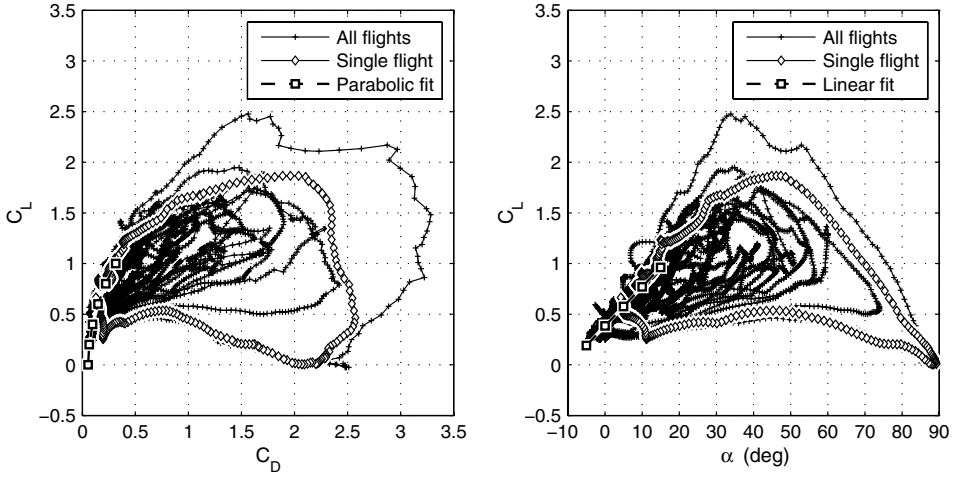

a) b)

Fig. 15 Experimentally determined a) drag polar and b) lift coefficients for the unsteady flights.

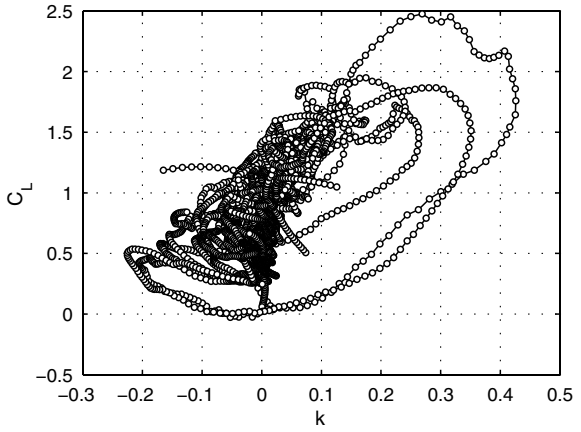

Fig. 16 Lift coefficient as a function of k for the unsteady flights.

negative values of k during stall recoveries (pitch-down) decreased C_L as expected from theoretical solutions to highly unsteady flow [21]. Figure 15a shows C_D varying from less than 0.1 during nominal gliding flight to above 2 during a number of flights that included aggressive, high angle-of-attack stall maneuvers. Although the nominal steady-state drag for a finite flat plate perpendicular to the flow is approximately 1.15 [27], unsteady effects have been shown to increase the drag coefficient [28].

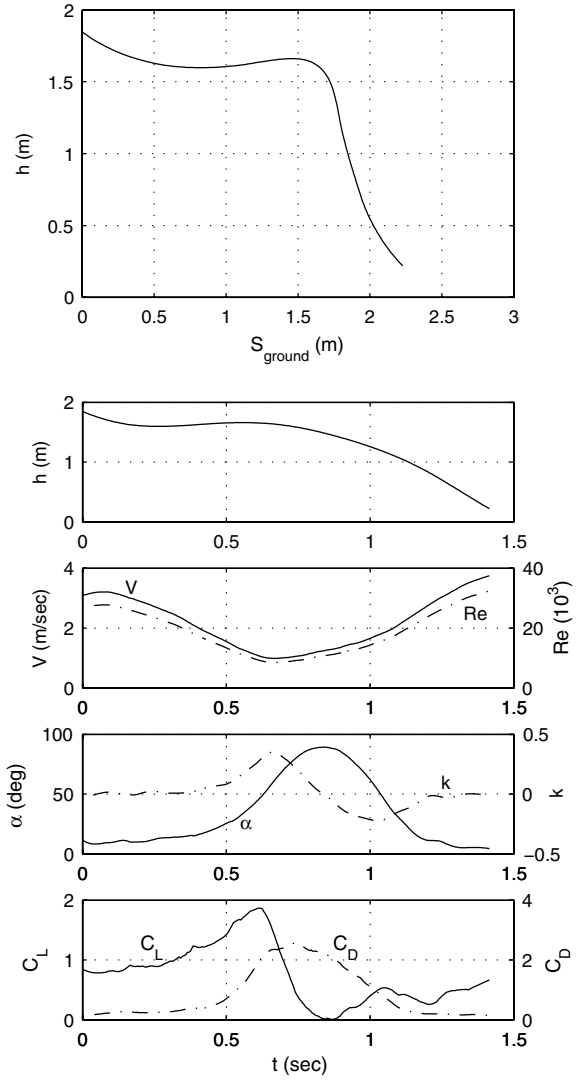

Fig. 17 The flight trajectory of the single flight along with the time history of various parameters.

One flight was selected to show the progression of an unsteady flight with an aggressive stall. The selected flight, shown by diamonds in Fig. 15, begins at an angle of attack of approximately 10 deg and progresses in the clockwise direction through a dynamic stall hysteresis loop. Figure 17 shows the trajectory and time history of selected flight parameters. As seen in the trajectory, the airplane entered into an aggressive stall by pitching up rapidly. During this time, the airspeed decreased. At 0.6 s, C_L peaked at a value of just less than 2, and at 0.66 s, k peaked at 0.35. The angle of attack continued to increase, but C_L decreased because the wing began to enter deep stall. From 0.75 to 1 s, the angle of attack was near 90 deg, which caused C_L to be close to zero. After reaching the peak angle of attack (near ≈0.8 s), C_L increased during the stall recovery dive. The flight had a large variation in C_L during the aggressive stall, which illustrates the influence that large unsteady effects can have on the lift coefficient during a high angular rate and high angle of attack flight.

The progression of C_D during the initial rapid increase in α follows a parabolic trend as shown in the drag polar (Fig. 15a). After the peak C_L at 0.6 s, the drag remains high as the lift decreases because the angle of attack continues to increase. Figure 17 shows that the C_D peak lags behind the reduced frequency, and that during the stall recovery, the drag coefficient remains high in a deep stall. The drag remains high as the flow transitions from completely separated at high angles of attack to reattached at low angles of attack. Once unsteady effects become small as both k and the angle of attack neared zero (near ≈1.25 s), the drag decreases to the steady-state C_D again.

To better understand the unsteady effects on lift, the lift coefficient data in Fig. 15b can alternatively be plotted as a smoothed contour depending on α and k, which is shown in Fig. 18. For $k = 0$ in Fig. 18 (the steady-state condition), C_L increases with the angle of attack until approximately $\alpha = 45$ deg, where C_L is 1.2 after which C_L decreases to almost zero at $\alpha = 90$ deg. The lift behavior described follows the expected C_L vs α curve for steady-state conditions, but as previously mentioned, when including the large unsteady effects, the range of C_L values becomes much larger and depends on k. For example, at $\alpha \approx 35$ deg, Fig. 15b shows that C_L varies from ≈0.3 to 2.5, and Fig. 18 shows that the C_L variation for the same angle of attack depends on k, which varies from ≈ -0.22 to 0.30. Figure 18 shows that the range of k and the influence of k changes over the range of angles of attack during the maneuver. Even at lower angles of attack, the increase in the range of k in the unsteady flight data over the previously shown quasi-steady flight data can be seen when comparing the variation of C_L. For example, during the unsteady flights at $\alpha = 10$ deg, the range of k is larger (−0.15 to 0.15) than was seen in the quasi-steady flights (−0.03 to 0.03), and subsequently

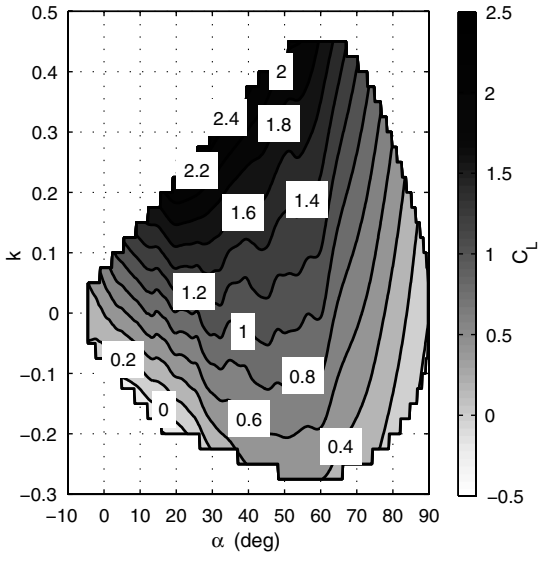

Fig. 18 C_L as a function of α and k for the unsteady flights.

C_L varies from zero to almost 1.6, which is quite large when compared with the quasi-steady results.

MAV flight can cover a larger flight envelope than full-sized airplanes and can include high angle of attack flight similar to the unsteady results shown here during maneuvers, such as perching [14,29], deep stall maneuvers, or highly dynamic flight in confined spaces. The unsteady results in Fig. 15 show the significant influence that unsteady aerodynamics can have on both the airplane lift and drag during rapid maneuvers. Figure 18 shows that during stall maneuvers the unsteady effect of k is largest close to the stall angle of attack and $C_{L_{\max}}$. In the range from $\alpha = 20$ to 50 deg, unsteady effects can have a large influence on lift as illustrated by the maximum C_L, which was $\approx$1.2 in the steady-state condition and increased well above 2 in the unsteady case. However, the influence of k diminished during high angle of attack flight in a deep stall ($\alpha > 70$ deg). Figure 18 shows that the range of C_L becomes smaller at a high angle of attack and that the C_L variation as a function of k reduces as the angle of attack approaches 90 deg.

V. Conclusions

Position and attitude time histories of a low Reynolds number, unpowered micro air vehicle (MAV) were obtained from a motion tracking system and used to determine the longitudinal aerodynamic characteristics in quasi-steady flight and also unsteady high angle of attack flight, as might be experienced in perching, deep stall maneuvers, and highly dynamic flight in confined spaces. For quasi-steady flight, the aerodynamics followed the expected steady-state low Reynolds number behavior with an almost linear lift curve up to stall and a drag polar that was well captured by a parabolic drag polar fit. For the highly dynamic, high angle of attack flights that included deep stall, large dynamic stall hysteresis loops were observed during the motion that proceeded from pitch-up, to stall, and then recovery. At its peak, the lift coefficient reached a maximum value near 2.5, but typical values during dynamic maneuvers were near 2, which exceeded the nominal gliding flight $C_{L_{\max}}$ of approximately 1 for the thin cambered membrane wing at the nominal cruise flight Reynolds number of 25,000. For the gliding flight motions considered, the unsteady lift contribution can in part be modeled as a function of the reduced frequency k, but additional unsteady contributions are present and must be related to additional factors, such as vortex shedding, apparent mass, dynamic wing flex, and the laminar separation bubble. For high angles of attack approaching 90 deg, C_L approached zero and showed diminished dependency on the reduced frequency k. The results of these tests show that any attempt to accurately model or control MAVs during rapid maneuvers and high angle of attack agile flight needs to include unsteady effects to accurately predict and model the full vehicle aerodynamic characteristics.

Acknowledgments

The authors thank Arjun H. Rao for his assistance in developing, testing, and refining the experimental methodology. The authors would also like to thank Gavin K. Ananda for the drawing in Fig. 1. Finally, the authors would like to thank the University of Illinois at Urbana–Champaign Aerospace Robotics and Control Group for sharing the testing resources used in this research.

References

[1] Mueller, T. J., *Fixed and Flapping Wing Aerodynamics for Micro Air Vehicle Applications*, edited by Muller, T. J., Vol. 195, Progress in Astronautics and Aeronautics, AIAA, Reston, VA, 2001.

[2] Torres, G. E., and Mueller, T. J., "Aerodynamic Characteristics of Low Aspect Ratio Wings at Low Reynolds Numbers," *Fixed and Flapping Wing Aerodynamics for Micro Air Vehicle Applications*, edited by Muller, T. J., Vol. 195, Progress in Astronautics and Aeronautics, AIAA, Reston, VA, 2001, pp. 115–141.

[3] Pelletier, A., and Mueller, T. J., "Low Reynolds Number Aerodynamics of Low-Aspect-Ratio, Thin/Flat/Cambered-Plate Wings," *Journal of Aircraft*, Vol. 37, No. 5, Sept. 2000, pp. 825–832. doi:10.2514/2.2676

[4] Torres, G. E., and Mueller, T. J., "Low-Aspect-Ratio Wing Aerodynamics at Low Reynolds Numbers," *AIAA Journal*, Vol. 42, No. 5, May 2004, pp. 865–873. doi:10.2514/1.439

[5] Selig, M. S., Guglielmo, J. J., Broeren, A. P., and Giguère, P., *Summary of Low-Speed Airfoil Data*, Vol. 1, SoarTech Publ., Virginia Beach, VA, 1995.

[6] Selig, M. S., Lyon, C. A., Giguère, P., Ninham, C. P., and Guglielmo, J. J., *Summary of Low-Speed Airfoil Data*, Vol. 2, SoarTech Publ., Virginia Beach, VA, 1996.

[7] Lyon, C. A., Broeren, A. P., Giguère, P., Gopalarathnam, A., and Selig, M. S., *Summary of Low-Speed Airfoil Data*, Vol. 3, SoarTech Publ., Virginia Beach, VA, 1998.

[8] Selig, M. S., and McGranahan, B., "Wind Tunnel Aerodynamic Tests of Six Airfoils for Use on Small Wind Turbines," National Renewable Energy Laboratory, NREL/SR-500-34515, 2004.

[9] Carmichael, B. H., "Low Reynolds Number Airfoil Survey," NASA CR-165803, 1981.

[10] Laitone, E. V., "Aerodynamic Lift at Reynolds Numbers Below 7×10^4," *AIAA Journal*, Vol. 34, No. 9, Sept. 1996, pp. 1941–1942. doi:10.2514/3.13329

[11] Spedding, G. R., and McArthur, J., "Span Efficiencies of Wings at Low Reynolds Numbers," *Journal of Aircraft*, Vol. 47, No. 1, Jan. 2010, pp. 120–128. doi:10.2514/1.44247

[12] Bauer, A. B., "The Laminar Airfoil Problem," *Eighth National Free Flight Society Symposium*, National Free Flight Society, Lake Charles, CA, 1975, pp. 40–45.

[13] Hoburg, W., and Tedrake, R., "System Identification of Post Stall Aerodynamics for UAV Perching," AIAA Paper 2009-1930, 2009.

[14] Cory, R., and Tedrake, R., "Experiments in Fixed-Wing UAV Perching," AIAA Paper 2008-7256, 2008.

[15] Rhinehart, M., and Mettler, B., "Extracting Aerodynamic Coefficients Using Direct Trajectory Sampling," AIAA Paper 2008-6899, 2008.

[16] Mettler, B., "Extracting Micro Air Vehicles Aerodynamic Forces and Coefficients in Free Flight Using Visual Motion Tracking Techniques," *Experiments in Fluids*, Vol. 49, No. 3, Sept. 2010, pp. 557–569. doi:10.1007/s00348-009-0803-6

[17] "Vapor RTF," http://www.e-fliterc.com/Products/Default.aspx?ProdID=pkz3300 [retrieved June 2010].

[18] *Vicon MX System, System Reference: Revision 1.7*, Vicon Motion Systems, Oxford, UK, 2007.

[19] Savitzky, A., and Golay, M. J., "Smoothing and Differentiation of Data by Simplified Least Squares Procedures," *Analytical Chemistry*, Vol. 36, No. 8, 1964, pp. 1627–1639. doi:10.1021/ac60214a047

[20] Klein, V., and Morelli, E. A., *Aircraft System Identification: Theory and Practice*, AIAA Education Series, AIAA, Reston, VA, 2006, pp. 1–180.

[21] Leishman, J. G., *Principles of Helicopter Aerodynamics*, Cambridge Aerospace Series, Cambridge Univ. Press, New York, 2000, pp. 302–309.

[22] Stevens, B. L., and Lewis, F. L., *Aircraft Control and Simulation*, 2nd ed., Wiley, Hoboken, NJ, 2006, pp. 1–112.

[23] "H6 Ball Bearing Optical Shaft Encoder," http://www.usdigital.com/assets/general/120_h6_datasheet_0.pdf [retrieved April 2012].

[24] Uhlig, D. V., and Selig, M. S., "Stability Characteristics of Micro Air Vehicles from Experimental Measurements," AIAA Paper 2011-3659, 2011.

[25] Roskam, J., *Airplane Flight Dynamics and Automatic Flight Controls, Part I*, DAR Corp., Lawrence, KS, 1995, pp. 198–210.

[26] Phillips, W., *Mechanics of Flight*, 2nd ed., Wiley, Hoboken, NJ, 2009, pp. 339–440.

[27] Hoerner, S. F., *Fluid-Dynamic Drag*, 2nd ed., Published by S. F. Hoerner, Bakersfield, CA, 1965, p. 16, Chap. 3.

[28] Dickinson, M. H., and Götz, K. G., "Unsteady Aerodynamic Performance of Model Wings at Low Reynolds Number," *Journal of Experimental Biology*, Vol. 174, No. 1, 1993, pp. 45–64.

[29] Paranjape, A. A., Kimy, J., Gandhiz, N., and Chung, S.-J., "Experimental Demonstration of Perching by an Articulated Wing MAV," AIAA Paper 2011-6403, 2011.